Structure of synthetic K-rich birnessite obtained by high-temperature decomposition of KMnO4. I. Two-layer polytype from 800C experiment.

Anne-Claire Gaillot, David Flot, Victor.A. Drits, Alain Manceau, Manfred Burghammer, Bruno Lanson

Structure of synthetic K-rich birnessite obtained by high-temperature decomposition of $KMnO_4$.

I. Two-layer polytype from 800°C experiment.

Anne-Claire Gaillot[1], David Flot[2], Victor A. Drits[1,3], Alain Manceau[1], Manfred Burghammer[2], Bruno Lanson[1,*]

1 – Environmental Geochemistry Group, LGIT – Maison des Géosciences, University of Grenoble – CNRS, 38041 Grenoble Cedex 9, France.

2 – European Synchrotron Radiation Facility, BP 220, 38043 Grenoble Cedex, France

3 – Geological Institute, Russian Academy of Sciences, 7 Pyzhevsky street, 109017 Moscow, Russia

* Author to whom correspondence should be addressed.

e-mail: Bruno.Lanson@obs.ujf-grenoble.fr

Abstract

The structure of a synthetic potassium birnessite (KBi) obtained as a finely dispersed powder by thermal decomposition of $KMnO_4$ at 800°C was for the first time studied by single crystal X-ray diffraction (XRD). It is shown that KBi has a two-layer cell with a = 2.840(1) Å, and c = 14.03(1) Å, and space group $P6_3/mmc$. In contrast to the structure model proposed by Kim et al.,[1] the refined model demonstrates the sole presence of Mn^{4+} in the octahedral layers, the presence of 0.12 vacant layer sites per octahedron being responsible for the layer charge deficit. This layer charge deficit is compensated for 1) by the presence of

interlayer Mn^{3+} above or below vacant layer octahedra sharing three O_{layer} with neighboring Mn_{layer} octahedra to form a triple-corner surface complex (^{VI}TC sites), and 2) by the presence of interlayer K in prismatic cavities located above or below empty tridentate cavities, sharing three edges with neighboring Mn_{layer} octahedra (^{VI}TE sites). As compared to the structure model proposed by Kim et al.,[1] this ^{VI}TE site is shifted from the center of the prismatic cavity towards its edges. A complementary powder XRD study confirmed the structure model of the main defect-free KBi phase and allowed to determine the nature of stacking disorder in a defective accessory KBi phase admixed to the defect-free KBi.

Introduction

Birnessite is a phyllomanganate, that is a manganese oxide containing predominantly Mn^{4+} cations assembled in layers of edge-sharing octahedra. A layer charge deficit arises from the presence within layers of Mn^{3+} cations and/or vacant layer octahedra and is compensated for by the presence of interlayer cations which are typically hydrolyzable cations in natural phyllomanganates.[2-9]

Despite the relatively low natural abundance of manganese, birnessite is ubiquitous in nature and plays an essential role in the geochemistry of soils and oceanic nodules.[8-19] This role originates from its remarkable cation exchange capacity,[20-24] sorption,[25-31] and redox properties.[32-42] In particular, because of its high affinity for pollutants, such as heavy metals and organic contaminants, this mineral plays a pivotal role in their fate in contaminated waters and soils.[16,40-53]

Even though in nature birnessite is typically disordered and occurs in finely dispersed state, monomineralic birnessites with an enhanced three dimensional (3D) ordering are easily synthesized under a variety of laboratory conditions.[1-3,15,54-62] Because some synthetic

varieties can be considered as analogs of the natural ones, they have been used to determine the structural mechanism of heavy metal sorption[31,40,51,63,64] and to investigate the structural modification of birnessite as a function of pH.[65]

Recently, synthetic birnessites have attracted additional attention, because of their electrochemical and magnetic properties.[54-57,66-70] Birnessite species rank among the promising cathode materials for secondary lithium batteries if their lamellar framework is stable during insertion/de-insertion cycling. Such K-rich birnessite (KBi) varieties have been synthesized from the thermal decomposition of $KMnO_4$,[1] as well as from the reduction of $KMnO_4$ under hydrothermal conditions.[54,55]

A comprehensive structural and chemical knowledge of KBi varieties obtained under contrasting synthesis conditions is relevant to understanding their properties and to complementing the few studies that were devoted to the structural analysis of KBi.[1,54,61] From these studies, idealized structure models have been determined for KBi. From the Rietveld refinement of the structure of KBi obtained by thermal decomposition of $KMnO_4$ at 800°C, Kim et al. concluded that their sample has a $P6_3/mmc$ space group with a two layer periodicity, and chemical formula $K_{0.30}MnO_{2.11}\cdot 0.60\ H_2O$.[1] The two-layer periodicity along the **c** axis results from the regular alternation of octahedral layers rotated with respect to each other by 180° and related by a mirror plane. However, Kim et al.[1] confined their attention "to obtain an approximate and simple structural model (space group, unit cell and layer structural model)" and many details of KBi actual crystal structure are still missing.

The present and the companion articles[71,72] intend to provide new insight on the structure of high-temperature KBi varieties synthesized according to the protocol of Kim et al.[1] These contributions describe the main crystal chemical features of KBi samples obtained at 700°C, 800°C and 1000°C and demonstrate the key influence of temperature on the KBi structure. For example, KBi samples synthesized at different temperatures differ by their i) layer

sequences, ii) sub- and super-cell parameters, iii) distributions of heterovalent Mn, and iv) distributions of interlayer K and vacant layer octahedra.

In the present article, the crystal structure of a KBi sample obtained at 800°C is studied by X-ray diffraction (XRD), X-ray absorption near edge structure (XANES) and extended X-ray absorption fine structure (EXAFS) spectroscopies, and thermal and chemical analyses. In contrast to previous structural characterizations of natural and synthetic birnessites, the structure refinement of our fine-grained KBi sample was performed for the first time on a single crystal using X-ray micro-diffraction, recently available on synchrotron radiation sources. KBi single crystal structural study was complemented by the simulation of the powder XRD pattern of the bulk sample. Powder diffraction confirmed the structure model of defect-free crystals and revealed the admixture of a defective KBi variety. The nature and content of stacking faults, which are common in birnessites, in this ancillary component were determined using a trial-and-error approach.

Experimental Section

Experimental methods. KBi sample was prepared by thermal decomposition of a fine-grained $KMnO_4$ powder (particle size < 50µm) following the procedure of Kim et al. Structural homogeneity of synthesis products was maximized by using flat crucibles containing a thin layer of $KMnO_4$ powder. Heating and cooling rates were set to 1°C per minute, pyrolysis occurring in the solid state for 5 hours in air, at 800°C. After decomposition and cooling, the final product was washed several times with bidistilled water (Milli-Q / 18.2 $M\Omega.cm^{-1}$) to reduce pH from 12-13 to about 9-10 and to remove soluble by-products such as K_2MnO_4 and K_3MnO_4. The black crystals of this KBi sample synthesized at 800°C, and

hereafter referred to as KBi_8, were then freeze-dried and stored under room conditions for chemical and structural characterizations.

Morphology of KBi_8 particles was examined by scanning electron microscopy (SEM) on a JEOL JSM 6320F high resolution SEM equipped with a field emission electron gun. KBi_8 consists predominantly of large micrometer-sized crystals exhibiting well defined crystallographic faces (Figure 1). The average dimensions of the monocrystals are 2 μm along the **c** axis and 6-10 μm within the **ab** plane, whereas the size of natural and synthetic low-temperature birnessites does not usually exceed 0.02 μm along the **c** axis and 1 μm within the **ab** plane.

Thermal analysis was carried out with a Netzsch Simultan STA409EP micro-analyzer with a heating rate of 10°C/min up to 1100°C. The weight loss due to structural water was measured by thermo-gravimetric analysis (TGA) and differential scanning calorimetry (DSC) on ~20 mg samples..

Total K and Mn contents were determined using a Perkin-Elmer Optima 3000 ICP-AES after digestion of about 8 mg of birnessite powder in 200 mL of 1% HNO_3 / 0.1% $NH_3OH.Cl$ matrix. The mean oxidation state of manganese in birnessite was determined by potentiometric titration using $(NH_4)_2Fe(SO_4)$ Mohr salt and sodium pyrophosphate.[73,74]

KBi chemical and structural formulae. The chemical formula of KBi obtained by combining the K/Mn ratio (y) and the mean oxidation state, $2x$, may be written as K_yMnO_w, where $w = (2x + y) / 2$. If m, n, p and q represent the amounts of Mn^{4+}, Mn^{3+}, Mn^{2+} and vacant layer sites (□), respectively, per octahedron these parameters are related by the following equations: $q = 1 - 2 / w$, $m + n + p = 1$, and $2p + 3n + 4m = 2x$. Because the initial oxidation state of Mn in $KMnO_4$ was +7, it is reasonable to assume that KBi_8 sample does not contain Mn^{2+} ($p = 0$). Experimental support to this hypothesis is given in the XANES Results section. Accordingly, KBi_8 chemical formula may be written as:

$K^{+}_{y}Mn^{4+}_{2x-3}Mn^{3+}_{4-2x}O_{(2x+y)/2}$, (1)

which can be transformed into the structural formula:

$K^{+}_{2y/w}(Mn^{4+}_{(4x-6)/w}Mn^{3+}_{(8-4x)/w}\square_{1-2/w})O_2$ (2)

Finally, the contents of structural water and hydroxyl groups can be added to this structural formula from the amounts of water released during thermal treatment.

X-ray diffraction. *Data collection - KBi_8 monocrystal*. Microdiffraction patterns on a KBi_8 monocrystal were recorded at the Microfocus beamline ID13 (European Synchrotron Radiation Facility - ESRF, Grenoble) using the ID13 microdiffractometer.[75,76] The X-ray beam produced using an undulator is monochromatized by a Si(111) double monochromator, focused by an ellipsoidal mirror, and finally collimated to ~4 μm in diameter.

KBi_8 powder was first dispersed onto a kapton foil and diffraction images were collected from several individual grains to select the best candidates for a full data collection procedure. Selected crystals were then mounted on a very fine borosilicate glass fiber. The combined use of an in-line microscope and of fine-tune motors allows one to center the selected crystal on the rotation axis within ~1 μm. As a second step, visualization of the focal spot on a scintillator using the same microscope allows one to put the selected crystal exactly into the beam.

Complete data collection was then performed on a ~3 x ~3 x ~1 μm^3 crystal with the oscillation technique (φ scans), using a two-dimensional mar CCD detector (~130mm diameter, 2048 x 2048 pixels and a 0.06445 x 0.06445 mm^2 pixel size) and an Oxford Cryostream device to keep the sample temperature at ~100 K. Data sets were recorded for two detector positions (0˚ and 40˚ tilts), first with the glass fiber axis approximately parallel to the sample rotation axis and then with the glass fiber mounted in a special sample holder allowing a 30º tilt with respect to the sample rotation axis. All four data sets were recorded (20-30s counting times per frame) with a 6º oscillation range and a sample-detector distance of ~42

mm (0° detector tilt) or ~ 73 mm (40° detector tilt). A minimum of 72 frames (446° sample rotation) were collected for each data set. The detector was tilted to 40° in the vertical plane to reach a ~0.55 Å resolution at λ = 0.729 Å. High-resolution was necessary because of the limited number of unique reflections in the space group previously reported for KBi.[1]

Structure solution and refinement. Recorded frames were indexed and the reflections integrated using the XDS software suite.[77] Lattice parameters (a = 2.840(1) Å, c = 14.030(6) Å) were refined from 1523 reflections with $I > 6\sigma(I)$. Even though minimum because of the small crystal size, absorption correction was applied to obtain similar integrated intensities from symmetry-equivalent reflections.[77] A total of 6727 reflections were recorded for a maximum resolution of $2\theta = 82.8°$. Finally, the structure model was refined from 153 unique reflections (out of 155 possible; completeness of 98.7 %) with SHELXL-97.[78]

Data collection - KBi powder. Powder XRD pattern was recorded using a Bruker D5000 powder diffractometer equipped with a Kevex Si(Li) solid state detector and $CuK\alpha_{1+2}$ radiation. Intensities were recorded at a 0.04° 2θ interval, from 5 to 90°, using a 40 sec counting time per step. A rotating sample holder was used to minimize the effect of preferential orientation.

Simulation of powder XRD patterns. One of the effective ways to determine the actual structure of layered minerals, and more especially of defective ones, is the calculation of powder XRD patterns using the mathematical formalism described by Drits & Tchoubar combined to a trial-and-error fitting procedure.[79] This method has been successfully used to determine the structure of natural and synthetic birnessites.[5,11,40,65,80] Details on the program used to simulate XRD patterns[81] and on the fitting procedure are given by Drits et al.[80] Calculations were restricted to 10ℓ reflections (35°-65° 2θ $CuK\alpha$ range) because these lines are most sensitive to some important structural parameters of layered minerals, including order/disorder in their stacking sequences, and site occupancies in both layer and interlayer.[82]

The background was assumed to be linearly decreasing over the angular range considered, and preferred orientation of particles was considered as a variable parameter. Quality of fit was estimated over the simulation range using the usual R_{wp} parameter.

XANES and EXAFS spectroscopy. Mn K-edge XANES and EXAFS spectra were collected at the LURE synchrotron radiation laboratory (Orsay – France) on the D42 spectrometer. The positron energy of DCI storage ring was 1.85 GeV and the current between 200 and 300 mA. The incident X-ray beam was monochromatized with a channel-cut Si(331) crystal. The absolute energy was pinned to the first inflection point of pure Mn (6539 eV). XANES spectra were normalized to unit step in the absorption coefficient from well below to well above the edge. EXAFS spectra were recorded over the 6400-7300 eV range. Samples were prepared for transmission measurement as homogeneous thin mounts having an absorption edge jump lower than 1.0. They were oriented to the magic angle in the X-ray beam to eliminate any texture effects originating from possible preferential orientation of KBi crystals.[83]

Experimental data were analyzed using the WinXAS software package.[84] Radial structure functions (RSFs) were calculated using a Bessel function to minimize the intensity of side lobes resulting from truncation effects in Fourier transforms of EXAFS spectra.[85] Manceau showed that the intensity of side lobes with this function represents about 5% of the intensity of main structural peaks.[86] This analytical treatment enhances the sensitivity to weak EXAFS contributions and, in the case of phyllomanganates, allows one to detect low amounts of Mn-Mn pairs from corner-sharing octahedra (i.e. interlayer Mn cations located above/below vacant layer octahedra).[40] Mn-O and Mn-Mn distances and the number of atoms in nearest O (CN_O) and Mn (CN_{Mn}) coordination shells were determined using experimental phase shift and amplitude function calculated from stoichiometric λ-MnO_2, in which Mn^{4+} is surrounded by six O atoms at 1.91 Å and six nearest Mn atoms at 2.84 Å.[87] Typical uncertainty on interatomic distances is ±0.02 Å and that on coordination numbers is ±1.0. RSFs are not

corrected for EXAFS phase-shifts, causing peaks to appear at shorter distances (R + ΔR, with ΔR ~ -0.4 Å) relative to the true near-neighbor distances (R).

Results

Structural formula. DTA curve of KBi_8 shows two sharp endotherms at 148°C and 925°C (Figure 2). The low-temperature one corresponds to the loss of weight related to interlayer H_2O, the amount of which is 6.7%, whereas the high-temperature feature possibly results from the reduction of Mn^{4+} cations, which are stabilized by the presence of interlayer K cations. The DTA curve also contains a small endotherm at ~370°C probably related to the dehydroxylation of layer OH groups and corresponding to the departure of 1.9% H_2O (Table 1). The loss of weight within the 60-120°C range is likely due to the departure of adsorbed water.

Chemical analyses showed that the atomic K/Mn ratio calculated from ICP data and the mean Mn oxidation state are equal to 0.24 and 3.92, respectively (Table 1). Using these values and the structural water weight losses the following structural formula is deduced:

$$K^{+}_{0.231}(Mn^{4+}_{0.885}Mn^{3+}_{0.077}\square_{0.038})O_2 \cdot 0.60H_2O \qquad (3)$$

Structure refinement of a KBi_8 microcrystal. Since our KBi_8 sample has similar powder XRD pattern and unit-cell parameters as those of the sample synthesized by Kim et al.,[1] the same two-layer structure model can be hypothesized. An idealized scheme of this model is drawn in Figure 3. The close-packing notation for this model is:

AbC a' CbA c' AbC…

where A and C represent the positions of layer oxygen atoms (O_{layer}), b the Mn_{layer} positions, and a' and c' the positions of interlayer K cations which are located above and

below empty tridentate layer cavities in the interlayer prisms formed by the O_{layer} from adjacent layers (irregular dashed line - Figure 3).

The origin of the unit cell is assumed to be in the b site. Because of the hexagonal layer symmetry, O_{layer} in the **ab** plane form equilateral triangles with their side lengths equal to the *a* parameter. Triangles formed by O_{layer} in the A and C sites are rotated around the **c** axis by (2n+1)60°. Therefore, adjacent layers in the structure should be related by a 6_3 axis passing through Mn_{layer}, by a mirror plane *m* passing through the **c** axis and the long diagonal of the layer unit-cell, and by a glide plane *c* passing through the short diagonal of the layer unit-cell. In addition, the structural model may have centers of symmetry located for example in the b sites and a mirror plane *m* parallel to the **ab** plane and passing through interlayer K. After integration of recorded intensities, possible space groups were $P3_1c$, $P\text{-}3_1c$, $P6_3mc$, $P\text{-}6_2c$, and $P6_3/mmc$ in agreement with the absence of reflections with $hh\overline{2h}\ell$ in the experimental XRD pattern. The structure model was first refined using the most symmetrical $P6_3/mmc$ space group in agreement with the structure model proposed.[1] The other four space groups were subsequently assessed and lead to structure models similar to that obtained using $P6_3/mmc$ space group. In particular, for the 3 non-centrosymmetric space groups it was impossible to reject the presence of a center of symmetry and the high symmetry $P6_3/mmc$ space group was thus preferred.

The structure model proposed by Kim et al. was used to start our refinement.[1] In this model all atoms, except O_{layer}, occupy special positions with Mn_{layer} and K located in the 2a (0,0,0) and 2c (1/3,2/3,1/4) positions, respectively. Only the z-coordinate of O_{layer}, which is located in the 4f site (2/3,1/3,*z*), needed to be refined in this initial model. It was first assumed that the layer thickness is 2.00 Å (z_{Olayer} = 0.070) as determined for different synthetic birnessites.[1,4,5,63,65,80] Occupancies of Mn_{layer} (0.96), O_{layer} (2.00) and K (0.24) were set

according to the structural formula determined for KBi_8 (Eq. 3). After this initial refinement, R_1 was equal to 8.9% (GoF = 2.74) for strong reflections [Fo > 4σ(Fo)].

After this initial attempt, the strongest peak in the difference-Fourier map lay in the interlayer region with coordinates (0,0,0.1523). The distance from this position to the three nearest O_{layer} is 2.00 Å, this distance being similar to the Mn_{layer}-O_{layer} bond length. From the chemical composition of KBi_8, the additional peak was assigned unambiguously to interlayer Mn cations ($Mn_{interlayer}$). To provide an octahedral coordination to $Mn_{interlayer}$ water molecules were introduced in the interlayer space in 2c sites (1/3,2/3,1/4), like interlayer K, the resulting $<H_2O$-$Mn_{interlayer}>$ being 2.14 Å. The resulting average distance between $Mn_{interlayer}$ and coordinated oxygen atoms (O_{layer} and H_2O - 2.07 Å) is compatible with $<Mn^{3+}$-O> reported in Mn^{3+}-bearing layer Mn oxides and oxi-hydroxides (2.040-2.045 Å).[88] It is likely that $Mn_{interlayer}$ results from the migration of Mn^{3+}_{layer} into the interlayer. This migration should be accompanied by the formation of the same amount of vacant layer octahedra capped by $Mn_{interlayer}$ as evidenced by the distance from the $Mn_{interlayer}$ site to the (0,0,0) position (2.14 Å), which is unrealistically short if the two sites are occupied simultaneously. From KBi_8 structural formula (Eq. 3), it is possible to deduce the number of vacant layer sites (0.12 per octahedron), and that of $Mn_{interlayer}$ and of associated H_2O (0.08 and 0.24, respectively). The new structural formula writes:

$$K^{+}_{0.231}Mn^{3+}_{0.077}(Mn^{4+}_{0.885}\square_{0.115})O_2 \cdot 0.60\ H_2O \qquad (4)$$

Including these two interlayer positions into the structure refinement significantly improved the quality of fit (R_1 = 8.2% - GoF = 1.22). From DTA results, the amount of H_2O is 0.60 per octahedron. 0.24 of these H_2O molecules are coordinated to $Mn_{interlayer}$, and it is likely that the remaining 0.36 H_2O molecules are coordinated to K. These latter H_2O molecules will be hereafter referred to as O3, whereas O_{layer} and H_2O molecules bond to $Mn_{interlayer}$ will be referred to as O1 and O2, respectively. Similarly, Mn_{layer} and $Mn_{interlayer}$ will

be referred to as Mn1 and Mn2. Initial location of O3 sites was determined from the strongest peak observed at this stage in the difference-Fourier map (0.2054,0.1027,1/4 - Site 6h) which lay in the interlayer region. In addition, interlayer K was moved from its original 2c position to a 6h one because of its unrealistically high thermal displacement factors (Ueq = 0.18). K1 and O3 positions were further refined and R_1 parameter was decreased to 5.2% (GoF = 0.78).

Further improvement of the fit was achieved by introducing anisotropic thermal displacement parameters for Mn1 and K. As a result, R_1 decreased to 2.75% (GoF = 1.09) for the 137 strong reflections [Fo > 4σ(Fo)], the value of this parameter being 3.3% when taking into account all 153 reflections. In the final step, 14 parameters were refined. Refined structural parameters of KBi_8 are listed in Table 2, atomic positions of layer and interlayer species are schematized in Figure 4, and selected interatomic distances are given in Table 3.

Indexing and simulation of the powder XRD pattern. Because it was difficult to find a monocrystal suitable to carry out the above structure refinement, that is a crystal showing defined diffraction spots at very high resolution, one may wonder about the representativity of the selected crystal. In addition to assessing the representativity of the studied monocrystal, and to characterizing the sample heterogeneity, a complementary structural study by powder XRD was undertaken on the same sample to determine the nature and content of stacking faults which are common in birnessites. Reflections of KBi_8 powder XRD pattern (Figure 5) were indexed using a two layer hexagonal (2*H*) unit-cell with a = 2.845 Å, c = 14.235 Å, $\alpha = \beta = 90°$, and $\gamma = 120°$. These parameters are similar to those obtained by Kim et al. (a = 2.842 Å, c = 14.16 Å, $\alpha = \beta = 90°$, and $\gamma = 120°$), and are consistent with our structure refinement.[1]

Even though the experimental XRD pattern recorded for KBi_8 exhibits a low background intensity and sharp reflections, the bulk structure of this sample was not refined using the Rietveld technique but rather determined by a trial-and-error fitting procedure on the powder

XRD pattern. Indeed, the presence of significant and asymmetrically broadened tails near the 10ℓ reflections of the main KBi_8 phase impeded the use of the Rietveld method (Figures 5, 6). This broadening is most likely induced by the presence in the sample of a second birnessite-like phase having a disordered structure. As a consequence, the complete structure determination should include this disordered KBi_{8d} phase in addition to the main ordered phase (KBi_{8o}).

Ordered KBi_{8o} phase. The atomic positions refined on the microcrystal (Table 2) were used as initial values for the simulation of the XRD pattern, and site occupancies were derived from the structural formula of KBi_8 (Eq. 4). Coherent scattering domains were supposed to have a disk-like shape with the mean disk radius equal to 550 Å, whereas mean and maximum numbers of layers in the disks were equal to 20 and 60, respectively. These parameters yielded a satisfactory agreement between experimental and calculated profiles (data not shown – R_{WP} = 12.7%). Optimal fit to the powder diffraction data (Figure 6a – R_{WP} = 11.8% - R_{EXP} = 3.0%) was obtained by slightly adjusting atomic positions. Note that the atomic positions obtained from this trial-and-error fit to experimental data (Table 4) are close to those obtained from the refinement on KBi_8 monocrystal.

Even though the KBi_{8d} contribution to the diffracted intensity is not negligible (Figure 6b), the trial-and-error procedure provides reasonable constraints on the KBi_{8o} structure model. For example, if K is located in the center of the interlayer prisms (1/3,2/3,1/4), as proposed by Kim et al., intensities calculated for 100 and 104 reflections of KBi_{8o} are significantly lower than experimental ones (Figure 7a – R_{WP} = 14.2%). In contrast, intensities of these two reflections are significantly higher than experimental ones if K is located in the center of the prismatic faces (Figure 7b – R_{WP} = 16.7%), or on the edges of these prisms (not shown).

In addition, the intensity of 103 and 106 reflections strongly depends on the number of interlayer Mn cations, and these reflections may be used to constrain the distribution of Mn^{3+} between layer (Mn1) and interlayer (Mn2) sites. If the calculation is performed assuming only 0.04 vacant layer site per octahedron (Eq. 3), the intensities calculated for 103 and 106 reflections are much lower than experimental ones (Figure 7c – R_{WP} = 18.1%), the best distribution of intensities being obtained for the cation distribution from Eq. (4) as for KBi_8 monocrystal.

Disordered KBi_{8d} phase. To complete the structural determination of the bulk KBi_8 sample, special attention was paid to the characterization of the disordered KBi_{8d} phase. Because well-defined stacking faults are common in natural and synthetic birnessites,[63,65,80] diffraction features resulting from the random interstratification of similar layers with different interlayer displacements were considered. Introduction of such well-defined stacking faults in the simulation significantly broadens *hkℓ* reflections, and shifts them from their nominal positions.[89] The first stacking mode considered was identical to that in the ordered KBi_{8o} structure (2*H*), adjacent layers being rotated with respect to each other by 180°. In the second stacking mode, adjacent layers had the same orientation and were shifted with respect to each other by one third of the long diagonal of the layer unit cell. Following this translation, the origin of the upper layer had coordinates (1/3, 2/3) in the **ab** plane relative to the origin of the lower layer. Such a layer sequence corresponds to a three-layer rhombohedral (3*R*) periodicity, the close-packing notation of which is:

$^{c'}AbC_{a'}\ ^{b'}CaB_{c'}\ ^{a'}BcA_{b'}$

where A,B,C and a,b,c, correspond to the O_{layer} and Mn_{layer} positions, respectively, whereas a', b', c' are the positions for interlayer K. Such a KBi phase with a 3*R* stacking sequence was obtained hydrothermally.[54,72] In randomly interstratified 2*H*/3*R* structures, 10ℓ/01ℓ reflections should be located between neighboring 10ℓ/01ℓ reflections of individual

2*H* and 3*R* phases (Figure 6c), the actual position depending on the relative proportions of each stacking sequence.[89] Diffraction patterns calculated for such mixed layered structures allowed us to reproduce the broad asymmetric tails near the 10ℓ reflections of the KBi_{8o} pattern. The optimum fit to the experimental KBi_8 XRD profile shown on Figure 6a includes the contribution of a randomly interstratified phase containing 60% of 2*H* fragments and 40% of 3*R* layer pairs (Figure 6c) in addition to the contribution of the ordered KBi_{8o} phase (Figure 6b). Composition and structure of layers and associated interlayers were assumed to be identical in both 2*H* and 3*R* layer fragments.

XANES spectroscopy. The position in energy and the shape of the Mn K-edge XANES spectra are characteristic of Mn valency as illustrated in Figure 8a by the comparison of Mn^{2+}-, Mn^{3+}-, and Mn^{4+}-reference compounds. The position of the main absorption edge occurs at ~6562 eV for tetravalent Mn, 6559-6560 eV for trivalent Mn, and 6551-6552 eV for divalent Mn. Since XANES spectra of mixed Mn-valency compounds are weighted average of these elementary contributions this spectroscopy should provide additional insight about the oxidation state of Mn in KBi_8 Note, however, that Mn^{3+} spectra have a hump at 6550-6551 eV, which should not attributed to the presence of Mn^{2+} impurity

The structures of synthetic triclinic Na-birnessite and hexagonal H-birnessite, hereafter referred to as NaBi and HBi, have been determined by X-ray and electron diffraction,[5,65,90] and EXAFS spectroscopy.[91] NaBi has a vacancy-free layer structure containing 69% Mn^{4+} and 31% Mn^{3+}, whereas the ideal cation composition of HBi at pH 5 is $Mn^{2+}_{0.055}Mn^{3+}_{0.233}Mn^{4+}_{0.722}$ per octahedron.[65] Accordingly, the Mn absorption edge spectrum of NaBi (Figure 8b – solid triangles) is clearly left-shifted relative to the ideal pure Mn^{4+} (Figure 8b – dotted-dashed line). In spite of the large proportion of Mn^{3+} cations in the structure (0.31 per octahedron), no shoulder is visible at 6550-6551 eV. The edge crest for HBi-pH5 (Figure 8b – crosses) is slightly right-shifted relative to NaBi closer to 6562 eV, in

agreement with the higher proportion of Mn^{4+} cations in the hexagonal form. Two shoulders are now visible, one at 6559 eV in agreement with the presence of Mn^{3+} cations, and another at 6551-6552 eV which may be attributed to Mn^{2+} owing to the absence of this feature in NaBi. The reduced normalized intensity of the edge resonance in HBi is also consistent with a higher mixed-valency of Mn in this sample.

It is then possible to assess Mn valency in KBi_8 by comparison with the Mn absorption edges exhibited by these two birnessite samples. First, in KBi_8, the position of the absorption edge (6562 eV) and the high normalized absorbance at the edge crest plead for a high proportion of Mn^{4+} in agreement with the average oxidation state of Mn measured by titration in this sample (3.92). Also, no hump is observed at ~6552 eV as expected if Mn^{2+} cations were present in significant amount. On the basis of titration measurement, the maximum proportion of Mn^{2+} is 0.04. Since this value is close to that in HBi-pH5 (0.05), which exhibits a shoulder at ~6552 eV, we can conclude that Mn^{3+} is the only low-valent form of Mn atom in KBi_8.

EXAFS spectroscopy. EXAFS data for KBi_8 are first compared to those of NaBi and HBi. Then, interatomic distances and number of atoms in nearest shells around Mn atoms are calculated from the simulation of EXAFS data.

In the NaBi structure Mn^{3+} cations are segregated in rows along the **b** axis, each Mn^{3+} row alternating with two Mn^{4+} rows in the perpendicular direction. Mn^{3+} octahedra are elongated because of the Jahn-Teller distortion and have a unique azimutal orientation resulting in an orthogonal layer symmetry and, at the local scale, in a distribution of Mn-Mn distances across octahedral edges (Table 5).[91] The ideal structural formula of HBi at pH 4 is $H^{+}_{0.333}Mn^{3+}_{0.123}Mn^{2+}_{0.043}(Mn^{4+}_{0.722}Mn^{3+}_{0.111}\square_{0.167})O_2(OH)^{-}_{0.013}\cdot 0.49H_2O$,[65] where cations within the parentheses are in the layer and those outside are in the interlayer. Interlayer Mn^{3+} results from the migration of layer Mn^{3+} during the NaBi-to-HBi transformation at low pH.

As a result, Mn-Mn distances in the layer are less scattered in HBi than in NaBi, and the presence of octahedrally coordinated Mn^{2+} and Mn^{3+} above/below vacant layer sites leads to the presence of a corner-sharing Mn-Mn shell at about 3.52 Å (Table 5).

These structural differences between NaBi and HBi are well apparent on EXAFS spectra and RSFs (Figure 9a). Comparison of the modulus and imaginary parts of the Fourier transforms of NaBi and HBi indicates that the nearest Mn-Mn shell at $R + \Delta R = 2.5$ Å, corresponding to edge-sharing contributions, is significantly expanded in NaBi because of the higher amount of layer Mn^{3+}, whereas HBi possesses a characteristic peak at $R + \Delta R = 3.10$ Å from the corner-sharing Mn-Mn shell. Another difference between NaBi and HBi is the decrease of the amplitude of the first RSF peak in HBi due to the wider distribution of Mn-O distances caused by the mix of Mn atoms in layer and interlayer sites and their coordination to only O ligands in NaBi and to O, OH and H_2O ligands in HBi. EXAFS spectra and RSFs obtained for KBi_8 and HBi are essentially the same, indicating that Mn has a similar local structure in the two phyllomanganates. The two spectra have the same frequency but a significantly distinct shape in the 4-7 $Å^{-1}$ range (arrows - Figure 9b). This observation suggests that the mean Mn-O and Mn-Mn distances are the same in the two structures, but that Mn has a slightly different coordination chemistry. The comparison of RSFs shows that the first peak has a higher amplitude and the third peak a lower amplitude in KBi_8 compared to HBi. More coherent Mn-O distances account for the enhancement of the first RSF peak whereas the decreased number of Mn_{layer}-$Mn_{interlayer}$ pairs, which is consistent with a lower proportion of Mn^{3+} in the interlayer of KBi_8 as indicated by XRD, explains the reduction of the third RSF peak.

Results from the least-squares fits of the contribution to EXAFS spectra of Mn-Mn shells for KBi_8 are compared to NaBi and HBi in Table 5. Good agreement between theory and data over the fit range was obtained assuming a single shell at 2.87 Å for KBi_8, and two shells at

2.88 Å and 3.52 Å for HBi. The short distance shell corresponds to Mn_{layer}-Mn_{layer} pairs and the higher distance to Mn_{layer}-$Mn_{interlayer}$ pairs. The addition of a Mn_{layer}-$Mn_{interlayer}$ shell in the simulation for KBi_8 did not improve statistically the spectral fit, although XRD results and the examination of RSFs gave supportive evidence for its existence. The average number of Mn_{layer}-$Mn_{interlayer}$ pairs can be calculated from the structural formula as the weighted sum of the different coordination environments:

$$CN_{corner} = \sum_i W_i \, CN_i, \qquad (5)$$

where i refers to Mn site, W_i to Mn site occupancy, and CN_i to the number of Mn neighbors for site i. For KBi_8 (Eq. 4), CN_{corner} = 0.885 x (0.077/0.115) + 0.077 x 6.0 = 1.1, and for HBi, CN_{corner} = 0.833 x 1.0 + 0.167 x 6.0 = 1.8. The former value is equal to the detection limit of corner-sharing Mn octahedra in phyllomanganates by EXAFS spectroscopy,[40] and the latter almost twice as high.

Discussion

The structure model proposed for KBi_8 differs substantially from that refined by Kim et al.[1] First, in the new model interlayer K is not located in the center of a prismatic cavity (2/3,1/3,1/4) but in a split 6h position (0.227,0.113,1/4). Second, interlayers of KBi_8 contain Mn^{3+} and K^+ cations, instead of only K^+ in the former model. Third, the manganese layer contains only Mn^{4+} cations and a significant amount of vacant sites. Finally, the positions of interlayer water molecules and their occupancies were identified. These structural features are discussed below.

KBi_8 layer. As in other phyllomanganates, the length of shared edges (2.567 Å - all distances are from the single crystal refinement) is significantly shorter than that of unshared edges (2.840 Å). The Mn-O bond length (1.914 Å) is consistent with the sole presence of

Mn^{4+} cations in KBi_8 layers as this value is typical for MnO_2 compounds.[87,92] The bond-valence calculation presented in Table 6 is also consistent with this conclusion. As a result, vacant octahedra represent the sole source of layer charge deficit in KBi_8. The presence of vacant layer sites is supported by micro-crystal XRD structure refinement, trial-and-error simulation of powder XRD pattern and EXAFS spectroscopy. Given that in layered structures vacant and occupied octahedral sites have different size and shape, atomic positions listed in Table 2 are average values. This approximation may account for the small deviations observed between calculated and expected bond valence values.

KBi_8 interlayer. According to XRD and EXAFS results, $Mn_{interlayer}$ (Mn2) is located above/below vacant layer sites. The three O_{layer} (O1) atoms from these vacant octahedra provide half of the Mn2 octahedral coordination which is completed by H_2O molecules (O2). Mn2 site is shifted from the center of the octahedron towards O1 atoms, leading to <d(Mn2-O1)> (1.989 Å) shorter than <d(Mn2-O2)> (2.152 Å). These distances are consistent with Mn^{3+}-O and Mn^{3+}-H_2O bond lengths, respectively, whereas they would be unrealistically short for Mn^{2+}-O and Mn^{2+}-H_2O distances, since Mn^{2+} is ~0.1 Å bigger than Mn^{3+}.[92] The mean Mn2-O distance (2.07 Å) is slightly larger than <Mn^{3+}-O> (2.04 Å) reported for Mn^{3+}-bearing oxides and oxi-hydroxides.[88] In addition, interlayer O2 atoms form weak H-bonds with nearest O_{layer} atoms from the adjacent layer (<d(O1-O2)> across the interlayer equals 3.006 Å - Table 3).

Table 6 shows that Mn^{3+} cations in Mn2 sites are slightly undersaturated as they receive only 2.66 valence unit (v.u.). As a consequence, an additional refinement step was performed by setting the O2 site in a 6h position. The refined O2 position (0.212, 0.606, 1/4) results in a shorter Mn2-O2 distance (2.060 Å) and thus provides a better charge compensation to Mn^{3+} cations, which then receive 2.94 v.u. However, this additional step did not improve the quality of fit (R_1 = 2.74% - GoF = 1.12). In addition, all attempts to describe the Jahn-Teller

distortion of Mn^{3+} octahedra by setting the Mn2 site, and possibly the O2 one, in a 12k position failed. This may be due to the random orientation of the elongated diagonal of the distorted Mn^{3+} octahedra and, consequently Mn2 and O2 positions are averaged in Table 2. Bond-valence calculations performed assuming the presence of Mn^{2+} in the Mn2 site lead to unrealistically high positive charge values (3 x 0.584 + 3 x 0.376 = 2.88 v.u.). The absence of Mn^{2+} inferred from bond valence calculations are in complete agreement with the Mn valency determined by XANES spectroscopy.

As can be seen in Figure 10, within the prisms formed by O_{layer} atoms from adjacent layers and topped on either side by empty tridentate cavities, K occupies with equal probability one of the three possible sites shown on Figure 4a. With respect to the position given by Kim et al. these three sites are shifted towards the edges of the prism, staying at equal distance from the two adjacent layers (z = 1/4).[1] In this site, interlayer K is coordinated to the four O_{layer} atoms from the nearest face of the prism and to two H_2O molecules located in O3 sites, these six atoms defining a distorted octahedron (Figures 4, 10). <K-O1> and <K-O3> distances are equal to 2.907 Å and 3.250-3.428 Å, respectively, and their average (3.05 Å) is typical for K in six-fold coordination.[92] The bond-valence calculation (Table 6) shows that this first octahedral shell compensates only part of the K^+ charge (0.57 v.u.), the remainder being partially compensated by the next-nearest O-shell (0.19 v.u.). The short distance (2.743 Å) between H_2O molecules located in the O3 site and the nearest O_{layer} allows for the formation of strong H-bonds, with a favorable O1-O3-O1 angle of ~133° (Figure 4).

Migration of Mn^{3+} and origin of vacant layer sites. Structure models of synthetic birnessite-like species obtained at high pH and containing contrasting proportions of Mn^{3+} indicate that the behavior of this cation depends on its concentration within the Mn layer. NaBi,[5,90] CaBi,[80] and KBi_{10} obtained from thermal decomposition of $KMnO_4$ at 1000°C[71] have high concentrations of Mn^{3+} (~1/3 of total Mn). In these three species, heterovalent

Mn_{layer} cations are segregated in Mn^{3+}- and Mn^{4+}-rich rows, and all Mn^{3+}-octahedra, which are elongated because of the Jahn-Teller distortion, present a unique azimutal orientation. These two features reduce the steric strains that would result from the random distribution of Mn^{3+}-octahedra, and lead to the departure from the hexagonal layer symmetry.

In contrast to NaBi, CaBi and KBi_{10}, KBi_8 contains only 0.08 Mn^{3+} cations per octahedron. It is thus likely that the local strains resulting from the distribution of Mn^{3+} as isolated cations compel these cations to migrate from layer to interlayer. The pure Mn^{4+}-containing layers are then devoid of strains and have a hexagonal symmetry. The presence of both K and Mn^{3+} in interlayers contributes to the cohesion between successive KBi_8 layers.

Local distribution of interlayer Mn and K. The presence of vacant layer sites in KBi_8 results in an uneven distribution of O_{layer} charges (Table 6) which is likely responsible for the shift of interlayer K off the center of interlayer prismatic cavities. Each of the three O_{layer} forming the roof of a vacant layer octahedron are coordinated to only two $Mn^{4+}{}_{layer}$ cations (Figure 10 – small open circles). These O_{layer} atoms receive 0.647 x 2 = 1.29 v.u., whereas O_{layer} coordinated to three Mn^{4+} receives 3 x 0.647 = 1.94 v.u. (Figure 10 – small solid circles). On one side of the vacant layer sites, the charge deficit of O_{layer} atoms is partly compensated by the presence of $Mn_{interlayer}$ as each O_{layer} is coordinated to two $Mn^{4+}{}_{layer}$ and one $Mn^{3+}{}_{interlayer}$, thus receiving 0.647 x 2 + 0.539 = 1.83 v.u. If no $Mn_{interlayer}$ is present, the neighboring prismatic cavity shares two edges with occupied Mn_{layer} sites and one with the vacant layer site. As a result, K hosted in these prismatic sites will likely shift towards the undersaturated edge to balance partially the charge deficit of the two undersaturated O_{layer}. According to our results this charge balance mechanism provides 0.123 v.u. to each O_{layer} (Table 6). As each vacant octahedron shares undersaturated edges with three prisms on either side of the layer, it is probable that each vacant site is neighbored by one K^+ cation on each side of the layer, if not capped on one side by $Mn_{interlayer}$. However, one may note that O_{layer}

atoms coordinated by two Mn_{layer} and one interlayer K remain strongly undersaturated (1.33-1.42 v.u.) and they likely hold a proton.

From the previous considerations, it is possible to estimate the number of K connected to vacant layer sites. First, 0.08 K should be bond to the 0.04 vacant octahedra per unit cell which are not capped by $Mn_{interlayer}$ (Eq. 4). Second, remaining vacant layer sites (0.08 per unit cell) share three corners on the one side with $Mn_{interlayer}$ octahedra and are neighbored by one K on the other side (Figures 4b, 10). Therefore, the 0.12 vacant layer sites should be neighbored by 0.04 x 2 + 0.08 = 0.16 K. The remaining 0.08 K are distributed within interlayer prisms which are not associated with vacant layer octahedra. In this case, the reason for the shift in position of K atoms is unclear. Note however that in 3*R* layer pairs the center of a tridentate cavity from one layer is superimposed with the Mn1 site of the adjacent layer. As a consequence, in 3*R* layer pairs the shift of K would decrease the electrostatic repulsion between interlayer K and Mn_{layer} from the next layer.

Origin of KBi_{8d} phase. The interstratified 3*R*/2*H* phase likely results from an heterogeneous heat distribution within the $KMnO_4$ layer during the synthesis. Gaillot et al. indeed showed that temperature is the main factor controlling the formation of KBi polytypes and interstratified phases.[72] Specifically, thermal decomposition of $KMnO_4$ at 700°C leads to the formation of 3*R*/2*H* phases in which 3*R* layer pairs prevail.

Acknowledgment. VAD is grateful to the Environmental Geochemistry Group of the LGIT (Grenoble, France) and to the Russian Science Foundation for financial support. BL and AM acknowledge financial support from INSU/Géomatériaux, CNRS/ACI "Eau et Environnement" and CNRS/PICS709 programs. Serge Nitsche (CRMC2 - Marseille), Céline Boissard (Hydr'ASA - Poitiers), Martine Musso and Delphine Tisserand (LGIT - Grenoble) are thanked for their technical support (SEM images, DT-TG analyses, and chemical

analyses, respectively). We are grateful to the LURE and to the ESRF (D42 and ID13 beamlines, respectively) for the provision of beam time, and to Agnès Traverse for her assistance during the EXAFS data collection.

Supporting Information Available: An X-ray crystallographic file (CIF). This material is available free of charge via the Internet at http://pubs.acs.org.

Figure captions

Figure 1. Scanning electron micrograph of KBi_8 particles.

Figure 2. Experimental DTA-TG and DSC traces obtained for KBi_8.

Figure 3. Idealized structure model for KBi_8 (modified from Kim et al.[1]). **a)** Projection on the **ab** plane. The upper surface of the lower layer is shown as light shaded triangles. O_{layer} and Mn_{layer} of this lower layer are shown as small solid and open circles, respectively. Large shaded circles = Interlayer potassium. **b)** Projection along the **b** axis. Open and solid symbols indicate atoms at y = 0, and at y = ±1/2, respectively. Large circles = O_{layer} atoms, small circles = Mn_{layer} atoms. Dotted-dashed lines outline the interlayer prisms defined by the two empty tridentate layer cavities. The center of these prisms is shown by regular dashed lines. **c)** Central projection. Dotted-dashed lines as in Figure 3b.

Figure 4. Structure model for KBi_8. **a)** Projection on the **ab** plane. Symbols as for Figure 3a. Mn1 and Mn2 cations are shown as large open circles. Interlayer H_2O molecules (O2 and O3) are shown as large open circles with a dashed outline. **b)** Projection along the **b** axis. Symbols as for Figure 3b. Large circles = Mn_{layer} atoms, small circles = O_{layer} atoms, large squares = vacant layer sites. Dotted-dashed lines outline the interlayer prisms defined by the two empty tridentate layer cavities. The center of these prisms is shown by dashed

lines, and the arrow outlines the shift of K cations from this ideal position. O1-O3-O1 angle (~133°) is outlined by a solid line.

Figure 5. Experimental powder XRD pattern obtained for KBi_8.

Figure 6. Comparison between experimental (crosses) and calculated (solid line) XRD patterns for KBi_8. Structural parameters used for calculation are listed in Table 4. **a)** Optimum model. The calculated pattern is the sum of a periodic KBi_{8o} phase and of a mixed layered KBi_{8d} phase (R_{WP} = 11.8%). **b)** Contribution of the KBi_{8o} phase. Arrows indicate the asymmetrically broadened tails near the 10ℓ reflections of the KBi_{8o} phase. **c)** KBi_{8d} is a mixed-layered structure containing 2*H* structural fragments (dashed line - similar to KBi_{8o}) and 3*R* layer pairs (solid line). The random interstratification of these two types of layer pairs (2*H*:3*R* = 60:40) induces the shift of the KBi_{8d} contribution from ideal 2*H* positions as indicated by horizontal arrows and leads to the diffraction pattern shown as a solid bold line.

Figure 7. Comparison between experimental and calculated XRD patterns for KBi_8. Patterns as for Figure 6. Arrows indicate the main misfits between experimental and calculated patterns. **a)** K is located in the center of the interlayer prisms (1/3, 2/3, 1/4) as suggested by Kim et al.[1] (R_{WP} = 14.2%). **b)** K is located on the faces (1/6, 5/6, 1/4) of the interlayer prisms (R_{WP} = 16.7%). **c)** All Mn atoms are located in layer octahedral sites resulting in a $K^{+}_{0.231}(Mn^{4+}_{0.885}Mn^{3+}_{0.077}\square_{0.038})O_2 \cdot 0.60H_2O$ structural formula (R_{WP} = 18.1%).

Figure 8. XANES spectra for reference compounds with a single Mn valency (Mn^{2+}, Mn^{3+} and Mn^{4+}), and for birnessite samples with a mixed Mn valency. **a**) The Mn^{2+} references are $MnCO_3$, and $Mn(OH)_2$, the Mn^{3+} references are Mn_2O_3 and β–MnOOH, and the Mn^{4+} reference is λ-MnO_2. The position of some characteristic spectral features are outlined as dotted-dashed line (Mn^{4+}), dashed lines (Mn^{3+}) and solid line (Mn^{2+}). **b**) XANES spectrum of KBi8 (solid line) together with low pH one–layer hexagonal birnessite (HBi,

dashed line) and triclinic birnessite (NaBi, open circles) references.[5,91] Other patterns as in Figure 8a.

Figure 9. k^3-weighted EXAFS spectra and Fourier transforms (modulus and imaginary parts) of k-weighted EXAFS spectra for KBi_8, and for low pH one–layer hexagonal birnessite (HBi) and triclinic birnessite (NaBi) references.[5,91]

Figure 10. Structure model for KBi_8. Projection on the **ab** plane. Symbols as for Figure 4a. Mn1 cations are shown as large solid circles. Dot-dashed lines outline the distorted octahedron defined by O1 and O3 coordinated to interlayer K. The lower surface of the layer is shown as dark shaded triangles. O_{layer} atoms coordinated to 3 Mn^{4+} cations are shown as small solid circles, whereas O_{layer} atoms coordinated to only 2 Mn^{4+} cations are shown as small open circles. Water molecules coordinating the Mn^{3+} cation in Mn_2 position below the vacant layer site are shown.

Table 1. Main chemical parameters of KBi_8 sample

	KBi_8
Weight loss[a] due to interlayer H_2O	6.72%
Weight loss[a] due hydroxyl groups	1.90%
K/Mn[b] ratio	0.240
Mn mean oxidation state	3.92

[a] Weight losses correspond to the 148°C and 370°C endotherms observed on the DTA-TG curves.
[b] K/Mn ratio was measured by ICP-AES.

Table 2. Atomic positions and occupancies for KBi_8 microcrystal

			x	**y**	**z**	**ζ(Å)**	**Occ.**[a]	**Ueq x 10^2 ($Å^2$)**[b]
Mn_{layer}	Mn1	2a	0	0	0	0	0.89	1.24(2)
O_{layer}	O1	4f	2/3	1/3	0.070(0)	0.98	1.00	1.73(4)
$Mn_{interlayer}$	Mn2	4e	0	0	0.151(1)	2.11	0.04	2.56(27)
K	K1	6h	0.227(6)	0.773(6)	1/4	3.51	0.08	9.44(95)
H_2O	O2	2c	1/3	2/3	1/4	3.51	0.23	8.25(212)
H_2O	O3	6h	0.226(13)	0.113(7)	1/4	3.51	0.12	4.70(72)

a = 2.840(1) Å, c = 14.03(1) Å. [a] Occupancies, which were set from the chemical analyses, are given for space group $P6_3/mmc$. [b] Anisotropic thermal displacements are U11 = U22 = $11.5(2)10^{-3}$, U33 = $14.1(3)10^{-3}$, U12 = $5.8(1)10^{-3}$, U23=U13 = 0 for Mn1, and U11 = U22 = $158.0(166)10^{-3}$, U33 = $8.2(18)10^{-3}$, U12 = $109.8(176)10^{-3}$, U23=U13 = 0 for K1.

Table 3. Selected inter-atomic distances[a] in KBi_8

	Microcrystal	**C.N.**	**Powder**
Mn1-Mn1	2.840(1)	6x	2.845
Mn_{layer}-O_{layer}	1.914(0)	6x	1.925
Height of Mn layer	1.96	-	2.00
Mn2-O1	1.989(0)	3x	1.993
Mn2-O2	2.152(0)	3x	2.176
Average Mn2-O	2.070	6x	2.084
Mn2-Mn1	3.540(1)	12x	3.555
O2-O1	3.006(1)	6x	3.038
K1-O1	2.907(1)	4x	2.947
Average $K_{interlayer}$-O_{layer}	3.051	6x	3.079
K1-O3	3.250(1)	1x	3.189
K1-O3	3.428(1)	2x	3.498
O3-O1	2.743(1)	2x	2.777

[a] All distances are given in Å.

Table 4. Atomic positions and occupancies for KBi_8 powder

			x	y	z	ζ(Å)	Occ.[a]	B[b]
Mn_{layer}	Mn1	2a	0	0	0	0	0.88	0.5
O_{layer}	O1	4f	2/3	1/3	0.070	1.00	1.00	1.0
$Mn_{interlayer}$	Mn2	4e	0	0	0.150	2.13	0.04	1.0
K	K1	6h	0.24	0.76	1/4	3.56	0.08	2.0
H_2O	O2	2c	1/3	2/3	1/4	3.56	0.24	1.5
H_2O	O3	6h	0.225	0.113	1/4	3.56	0.12	2.0

a = 2.845 Å, c = 14.235 Å. [a] Occupancies, which were set from the chemical analyses, are given for space group $P6_3/mmc$. [b] Thermal factors B were not refined. The proportions of random stacking faults in KBi_{8o} and KBi_{8d} are 6% and 20%, respectively. KBi_{8d} is a randomly interstratified mixed-layered structure of 2*H* and 3*R* layer pairs (60:40). Mean sizes of the coherent scattering domains along the **c** axis are 20 and 10 layers in KBi_{8o} and KBi_{8d}, respectively.

Table 5. EXAFS parameters for Mn-Mn pairs in birnessite samples and in the reference λMnO_2.

Sample	Fit interval ($Å^{-1}$)	Shells	R (Å)	CN[a]	σ^2 ($Å^2$)[b]	ΔE (eV)[c]	Resid.[d]	Free var.[e]
λMnO_2	3.7 < k < 13.5	1	2.85	6	29 10^{-4}	0.8	11	4
NaBi[f]	3.7 < k < 13.5	1	2.90	5.7	73 10^{-4}	-2.1	17	4
		2	2.88	3.6	33 10^{-4}[g]	-0.2[g]	12	6
			2.99	2.4	33 10^{-4}[g]	-0.2[g]		
HBi[f]	3.7 < k < 12	1	2.88	3.5	35 10^{-4}	0.5	21	4
		2	2.88	3.7	37 10^{-4}	0.8[g]	11	7
			3.52	2.2	90 10^{-4}	0.8[g]		
KBi_8	3.7 < k < 12	1	2.87	4.3	47 10^{-4}	-0.3	12	4

Typical uncertainty on interatomic distances is ±0.02 Å. [a] Coordination number. The scaling factor S_0^2 was calculated to obtain CN = 6 in the reference λMnO_2 (S_0^2=0.8). Typical uncertainty on coordination numbers is ±1.0. [b] Debye-Waller factor. [c] Variation of the energy threshold treated as a single adjustable parameter for all sub-shells. [d] Residual calculated from $R = [\sum|(k^3\chi_{exp} - k^3\chi_{cal})|/\sum|k^3\chi_{exp}|] \times 100$. [e] Number of variable parameters. In all fits, the number of independent variables, calculated by the Nyquist formula $2\Delta k\Delta R/\pi$,[93] was equal to 7. [f] EXAFS results are, within uncertainty, identical to those published by Silvester et al.[91] [g] Parameter varied but constrained equal for the two sub-shells.

Table 6. Empirical bond-valences (vu)[a] for KBi_8.

	O1[b]	O1[c]	O1[d]	O2	O3	Σ
Mn1	$0.647^{x6}\rightarrow$ $^{x3}\downarrow$	$0.647^{x2}\downarrow$	$0.647^{x2}\downarrow$			3.88
Mn2		$0.539^{x3}\rightarrow$		$0.347^{x3}\rightarrow$		2.66
K1	$0.041^{x2}\rightarrow$ $0.013^{x2}\rightarrow$		$0.123^{x4}\rightarrow$	$0.042^{x2}\rightarrow$	$0.049^{x1}\rightarrow$ $0.030^{x1}\rightarrow$	0.76
H^+	0.09[e] 0.04[f]			$0.788^{x2}\downarrow$	$0.788^{x2}\downarrow$	
Σ	1.94 - 2.03[g]	1.83	1.29 - 1.42[h]	1.92	1.61 - 1.62	

[a] Bond valences in v.u. (valence unit) calculated using the Valence for Dos program (v. 2.0 - http://www.ccp14.ac.uk/solution/bond_valence/index.html) and the parameters from Brese and O'Keeffe.[94] [b] O1 coordinated to 3 Mn^{4+} in Mn1. [c] O1 coordinated to 2 Mn^{4+} in Mn1 and 1 Mn^{3+} in Mn2. [d] O1 coordinated to 2 Mn^{4+} in Mn1. [e] O3-H-O1 H-bond. [f] O2-H-O1 H-bond. [g] Depending on whether this O1 receives additional valence from interlayer K^+ or H^+ through H-bond. [h] Depending on whether this O1 receives additional valence from interlayer K^+.

References cited

(1) Kim, S. H.; Kim, S. J.; Oh, S. M. *Chem. Mater.* **1999**, *11*, 557-563.

(2) Giovanoli, R.; Stähli, E.; Feitknecht, W. *Helv. Chim. Acta* **1970**, *53*, 209-220.

(3) Giovanoli, R.; Stähli, E.; Feitknecht, W. *Helv. Chim. Acta* **1970**, *53*, 453-464.

(4) Post, J. E.; Veblen, D. R. *Amer. Mineral.* **1990**, *75*, 477-489.

(5) Lanson, B.; Drits, V. A.; Feng, Q.; Manceau, A. *Amer. Mineral.* **2002**, *87*, 1662-1671.

(6) Manceau, A.; Gorshkov, A. I.; Drits, V. A. *Amer. Mineral.* **1992**, *77*.

(7) Manceau, A.; Gorshkov, A. I.; Drits, V. A. *Amer. Mineral.* **1992**, *77*, 1133-1143.

(8) Burns, R. G.; Burns, V. M. *Phil Trans Roy Soc London A* **1977**, *286*, 283-301.

(9) Chukhrov, F. V.; Gorschkov, A. I.; Rudnitskaya, E. S.; Sivtsov, A. V. *Izv. Akad. Nauk Geol.* **1978**, *9*, 67-76.

(10) Burns, V. M.; Burns, R. G. *Earth Planet. Sci. Lett.* **1978**, *39*, 341-348.

(11) Chukhrov, F. V.; Sakharov, B. A.; Gorshkov, A. I.; Drits, V. A.; Dikov, Y. P. *Int. Geol. Rev.* **1985**, *27*, 1082-1088.

(12) Drits, V. A.; Petrova, V. V.; Gorshkov, A. I. *Lithology and Raw Materials* **1985**, *3*, 17-39.

(13) Taylor, R. M.; McKenzie, R. M.; Norrish, K. *Aust. J. Soil Res.* **1964**, *2*, 235-248.

(14) Chukhrov, F. V.; Gorshkov, A. I. *Trans. Roy. Soc. Edinb. - Earth Sci.* **1981**, *72*, 195-200.

(15) Cornell, R. M.; Giovanoli, R. *Clays & Clay Miner.* **1988**, *36*, 249-257.

(16) McKenzie, R. M. *Aust. J. Soil Res.* **1967**, *5*, 235-246.

(17) Manceau, A.; Lanson, B.; Schlegel, M. L.; Harge, J. C.; Musso, M.; Eybert Berard, L.; Hazemann, J. L.; Chateigner, D.; Lamble, G. M. *Amer. J. Sci.* **2000**, *300*, 289-343.

(18) Manceau, A.; Tamura, N.; Marcus, M. A.; MacDowell, A. A.; Celestre, R. S.; Sublett, R. E.; Sposito, G.; Padmore, H. A. *Amer. Mineral.* **2002**, *87*, 1494-1499.

(19) Manceau, A.; Tamura, N.; Celestre, R. S.; MacDowell, A. A.; Geoffroy, N.; Sposito, G.; Padmore, H. A. *Environ. Sci. Technol.* **2003**, *37*, 75-80.

(20) Healy, T. W.; Herring, A. P.; Fuerstenau, D. W. *J. Colloid Interface Sci.* **1966**, *21*, 435-444.

(21) Le Goff, P.; Baffier, N.; Bach, S.; Pereira-Ramos, J.-P. *Mat. Res. Bull.* **1996**, *31*, 63-75.

(22) Murray, J. W. *J. Colloid Interface Sci.* **1974**, *46*, 357-371.

(23) Balistrieri, L. S.; Murray, J. W. *Geochim. Cosmochim. Acta* **1982**, *46*, 1041-1052.

(24) Stumm, W. *Chemistry of the solid-water interface and particle-water interface in natural systems*; Wiley: New York, 1992.

(25) Gray, M.; Malati, M. *J. Chem. Technol. Biotechnol.* **1979**, *29*, 127-134.

(26) Gray, M.; Malati, M. *J. Chem. Technol. Biotechnol.* **1979**, *29*, 135-144.

(27) Catts, J. G.; Langmuir, D. *Appl. Geochem.* **1986**, *1*, 255-264.

(28) Paterson, E.; Swaffield, R.; Clark, L. *Clay Miner.* **1994**, *29*, 215-222.

(29) Tu, S.; Racz, G. J.; Goh, T. B. *Clays & Clay Miner.* **1994**, *42*, 321-330.

(30) Appelo, C. A. J.; Postma, D. *Geochim. Cosmochim. Acta* **1999**, *63*, 3039-3048.

(31) Manceau, A.; Lanson, B.; Drits, V. A. *Geochim. Cosmochim. Acta* **2002**, *66*, 2639-2663.

(32) Oscarson, D. W.; Huang, P. M.; Liaw, W. K.; Hammer, U. T. *Soil Sci. Soc. Am. J.* **1983**, *47*, 644-648.

(33) Stone, A. T.; Morgan, J. J. *Environ. Sci. Technol.* **1984**, *18*, 617-624.

(34) Stone, A. T.; Ulrich, H. J. *J. Colloid Interface Sci.* **1989**, *132*, 509-522.

(35) Manceau, A.; Charlet, L. *J. Colloid Interface Sci.* **1992**, *148*, 425-442.

(36) Bidoglio, G.; Gibson, P. N.; O'Gorman, M.; Roberts, K. J. *Geochim. Cosmochim. Acta* **1993**, *57*, 2389-2394.

(37) Daus, B.; Mattusch, J.; Paschke, A.; Wennrich, R.; Weiss, H. *Talanta* **2000**, *51*, 1087-1095.

(38) Nico, P. S.; Zasoski, R. J. *Environ. Sci. Technol.* **2000**, *34*, 3363-3367.

(39) Silvester, E. J.; Charlet, L.; Manceau, A. *J. Phys. Chem.* **1995**, *99*, 16662-16772.

(40) Manceau, A.; Drits, V. A.; Silvester, E. J.; Bartoli, C.; Lanson, B. *Amer. Mineral.* **1997**, *82*, 1150-1175.

(41) Pizzigallo, M. D. R.; Ruggiero, P.; Spagnuolo, M. *Fresen. Environ. Bull.* **1998**, *7*, 552-557.

(42) Chorover, J.; Amistadi, M. K. *Geochim. Cosmochim. Acta* **2001**, *65*, 95-109.

(43) McKenzie, R. M. *Aust. J. Soil Res.* **1980**, *18*, 61-73.

(44) Majcher, E. H.; Chorover, J.; Bollag, J. M.; Huang, P. M. *Soil Sci. Soc. Am. J.* **2000**, *64*, 157-163.

(45) Pizzigallo, M. D. R.; Ruggiero, P.; Crecchio, C.; Mascolo, G. *J. Agr. Food Chem.* **1998**, *46*, 2049-2054.

(46) Taylor, R. M.; McKenzie, R. M. *Aust. J. Soil Res.* **1966**, *4*, 29-39.

(47) Wang, M. C.; Huang, P. M. *Soil Sci.* **2000**, *165*, 934-942.

(48) Baldwin, D. S.; Beattie, A. K.; Coleman, L. M. *Environ. Sci. Technol.* **2001**, *35*, 713-716.

(49) Farrell, R. E.; Huang, P. M.; Germida, J. J. *Appl. OrganoMetal. Chem.* **1998**, *12*, 613-620.

(50) Chao, T. T.; Theobald, P. K. *Econ. Geol.* **1976**, *71*, 1560-1569.

(51) Manceau, A.; Schlegel, M. L.; Chateigner, D.; Lanson, B.; Bartoli, C.; Gates, W. P. In *Synchrotron X-ray methods in clay science*; Schulze, D. G., Stucki, J. W., Bertsch, P. M., Eds.; Clay Minerals Society: Boulder, Co, 1999; Vol. 9, pp 68-114.

(52) Manceau, A.; Lanson, B.; Drits, V. A.; Chateigner, D.; Gates, W. P.; Wu, J.; Huo, D.; Stucki, J. W. *Amer. Mineral.* **2000**, *85*, 133-152.

(53) Manceau, A.; Drits, V. A.; Lanson, B.; Chateigner, D.; Wu, J.; Huo, D.; Gates, W. P.; Stucki, J. W. *Amer. Mineral.* **2000**, *85*, 153-172.

(54) Chen, R. J.; Zavalij, P.; Whittingham, M. S. *Chem. Mater.* **1996**, *8*, 1275-1280.

(55) Chen, R. J.; Chirayil, T.; Zavalij, P.; Whittingham, M. S. *Solid State Ionics* **1996**, *86-88*, 1-7.

(56) Ching, S.; Landrigan, J. A.; Jorgensen, M. L.; Duan, N.; Suib, S. L.; O'Young, C. L. *Chem. Mater.* **1995**, *7*, 1604-1606.

(57) Ching, S.; Petrovay, D. J.; Jorgensen, M. L.; Suib, S. L. *Inorg. Chem.* **1997**, *36*, 883-890.

(58) Ching, S.; Roark, J. L.; Duan, N.; Suib, S. L. *Chem. Mater.* **1997**, *9*, 750-754.

(59) Ching, S.; Suib, S. L. *Comment Inorganic Chem.* **1997**, *19*, 263-282.

(60) Herbstein, H. F.; Ron, G.; Weissman, A. *J. Chem. Soc. (A)* **1971**, 1821-1826.

(61) Kim, S. H.; Im, W. M.; Hong, J. K.; Oh, S. M. *J. Electrochem. Soc.* **2000**, *147*, 413-419.

(62) Yang, X. J.; Tang, W.; Feng, Q.; Ooi, K. *Cryst. Growth & Des.* **2003**, *3*, in press.

(63) Lanson, B.; Drits, V. A.; Gaillot, A. C.; Silvester, E.; Plancon, A.; Manceau, A. *Amer. Mineral.* **2002**, *87*, 1631-1645.

(64) Drits, V. A.; Lanson, B.; Bougerol Chaillout, C.; Gorshkov, A. I.; Manceau, A. *Amer. Mineral.* **2002**, *87*, 1646-1661.

(65) Lanson, B.; Drits, V. A.; Silvester, E. J.; Manceau, A. *Amer. Mineral.* **2000**, *85*, 826-838.

(66) Bach, S.; Henry, M.; Baffier, N.; Livage, J. *J. Solid State Chem.* **1990**, *88*, 325-333.

(67) Bach, S.; Pereira-Ramos, J. P.; Baffier, N. *J. Solid State Chem.* **1995**, *120*, 70-73.

(68) Bach, S.; Pereiraramos, J. P.; Baffier, N. *J. Electrochem. Soc.* **1996**, *143*, 3429-3434.

(69) Chen, J.; Bradhurst, D. H.; Dou, S. X.; Liu, H. K. *J. Electrochem. Soc.* **1999**, *146*, 3606-3612.

(70) Ching, S.; Krukowska, K. S.; Suib, S. L. *Inorg. Chim. Acta* **1999**, *294*, 123-132.

(71) Gaillot, A.-C.; Drits, V. A.; Lanson, B.; Manceau, A. *Amer. Mineral.*, In preparation.

(72) Gaillot, A.-C.; Drits, V. A.; Plançon, A.; Lanson, B. *Amer. Mineral.*, In preparation.

(73) Vetter, K. J.; Jaeger, N. *Electrochim. Acta* **1966**, *11*, 401-419.

(74) Lingane, J. J.; Karplus, R. *Ind. Eng. Chem. Anal. Ed.* **1946**, *18*, 191-194.

(75) Perrakis, A.; Cipriani, F.; Castagna, J. C.; Claustre, L.; Burghammer, M.; Riekel, C.; Cusack, S. *Acta Crystallogr. D - Biol. Cryst.* **1999**, *55 Part 10*, 1765-1770.

(76) Riekel, C.; Burghammer, M.; Flot, D. *Polymeric Materials: Science & Engineering* **2001**, *85*, 171-172.

(77) Kabsch, W. *J. Appl. Cryst.* **1993**, *26*, 795-800.

(78) Sheldrick, G. M.; Schneider, T. R. In *Methods in Enzymology*; Carter, C. W., Jr., Sweet, R. M., Eds.; Academic Press: San Diego, 1999; Vol. 277, pp 319-343.

(79) Drits, V. A.; Tchoubar, C. *X-ray diffraction by disordered lamellar structures: Theory and applications to microdivided silicates and carbons*; Springer-Verlag: Berlin, 1990.

(80) Drits, V. A.; Lanson, B.; Gorshkov, A. I.; Manceau, A. *Amer. Mineral.* **1998**, *83*, 97-118.

(81) Plançon, A. *J. Appl. Cryst.* **2002**, *35*, 377.

(82) Brindley, G. W. In *Crystal Structures of Clay Minerals and their X-ray Identification*; Brindley, G. W., Brown, G., Eds.; Mineralogical Society: London, 1980, pp 125-195.

(83) Manceau, A. *Phys. Chem. Miner.* **1990**, *17*, 363-370.

(84) Ressler, T. *J. Synchrotron Radiat.* **1998**, *5 Part 2*, 118-122.

(85) Manceau, A.; Combes, J. M. *Phys. Chem. Miner.* **1988**, *15*, 283-295.

(86) Manceau, A. *Geochim. Cosmochim. Acta* **1995**, *59*, 3647-3653.

(87) Thackeray, M. M.; de Kock, A.; David, W. I. F. *Mat. Res. Bull.* **1993**, *28*, 1041-1049.

(88) Shannon, R. D.; Gumeman, P. S.; Chenavas, J. *Amer. Mineral.* **1975**, *60*, 714-716.

(89) Drits, V. A.; McCarty, D. K. *Amer. Mineral.* **1996**, *81*, 852-863.

(90) Drits, V. A.; Silvester, E. J.; Gorshkov, A. I.; Manceau, A. *Amer. Mineral.* **1997**, *82*, 946-961.

(91) Silvester, E. J.; Manceau, A.; Drits, V. A. *Amer. Mineral.* **1997**, *82*, 962-978.

(92) Shannon, R. D. *Acta Crystallogr.* **1976**, *A32*, 751-767.

(93) Michalowicz, A.; Provost, K.; Laruelle, S.; Mimouni, A.; Vlaic, G. *J. Synchrotron Radiat.* **1999**, *6*, 233-235.

(94) Brese, N. E.; O' Keeffe, M. *Acta Crystallogr.* **1991**, *B47*, 192-197.

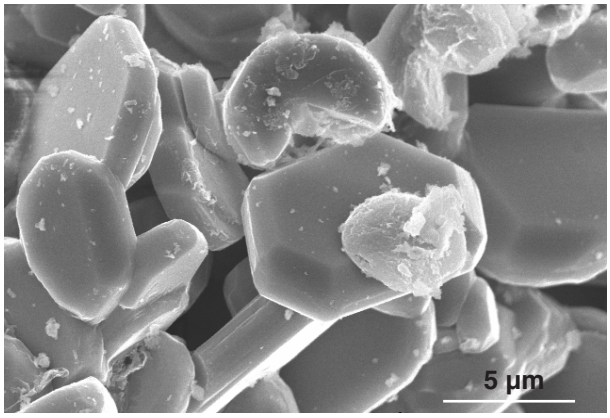

Please print in one column format

Gaillot et al. Fig.01

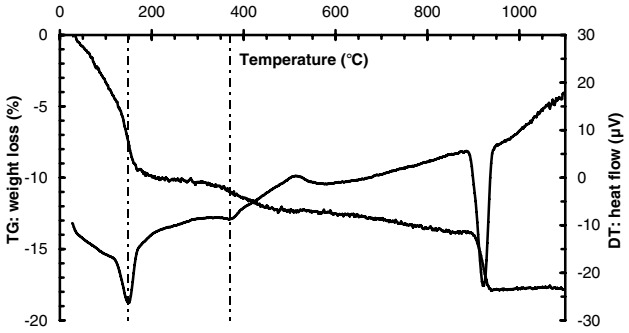

Please print in one column format

Gaillot et al. - Fig. 02

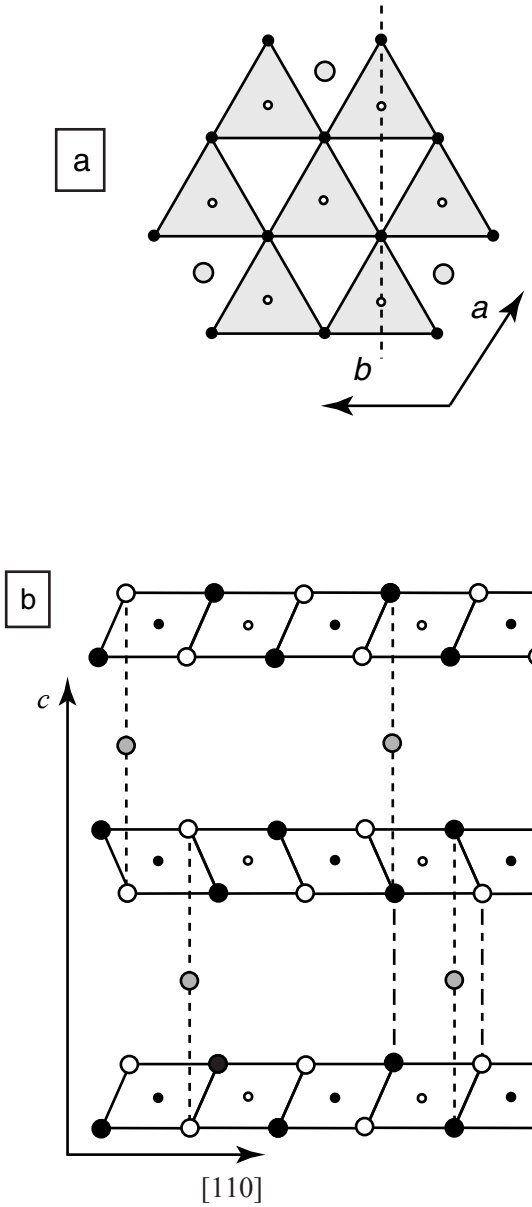

Please print in one column format

Gaillot et al. Fig. 03

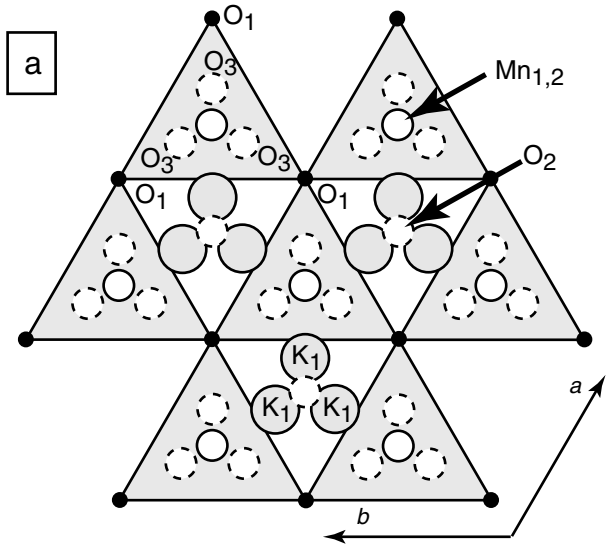

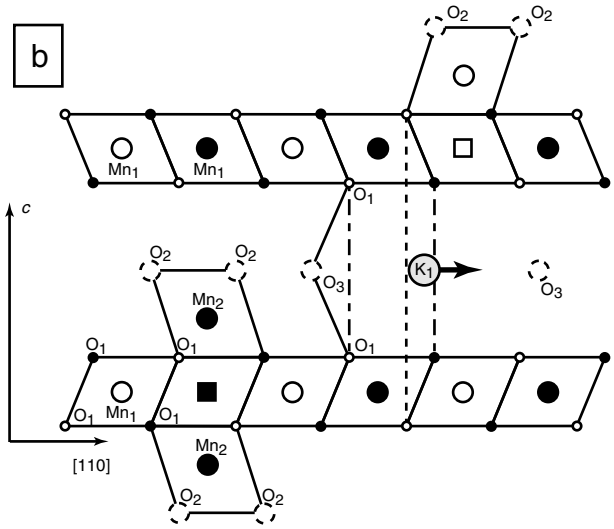

Please print in one column format

Gaillot et al. Fig. 04

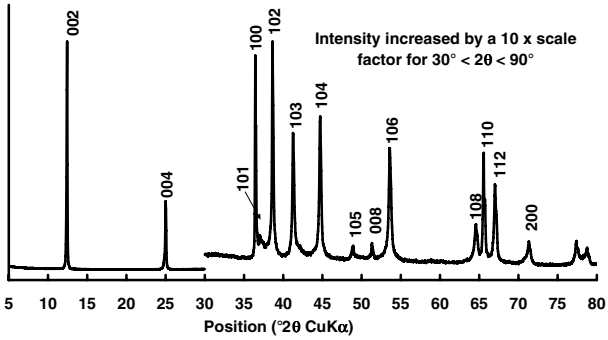

Please print in one column format

Gaillot et al. Fig. 05

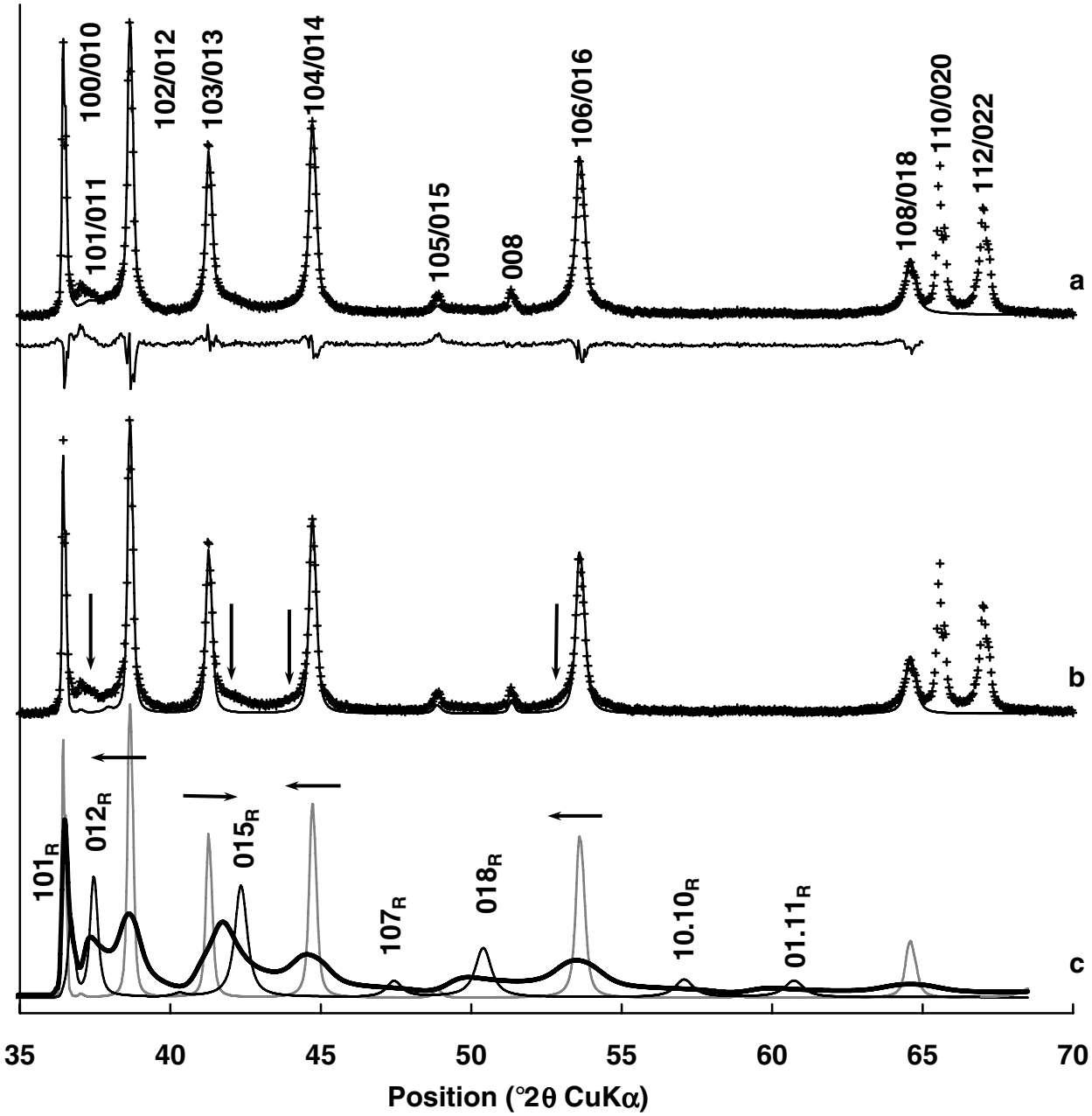

Please print in two column format

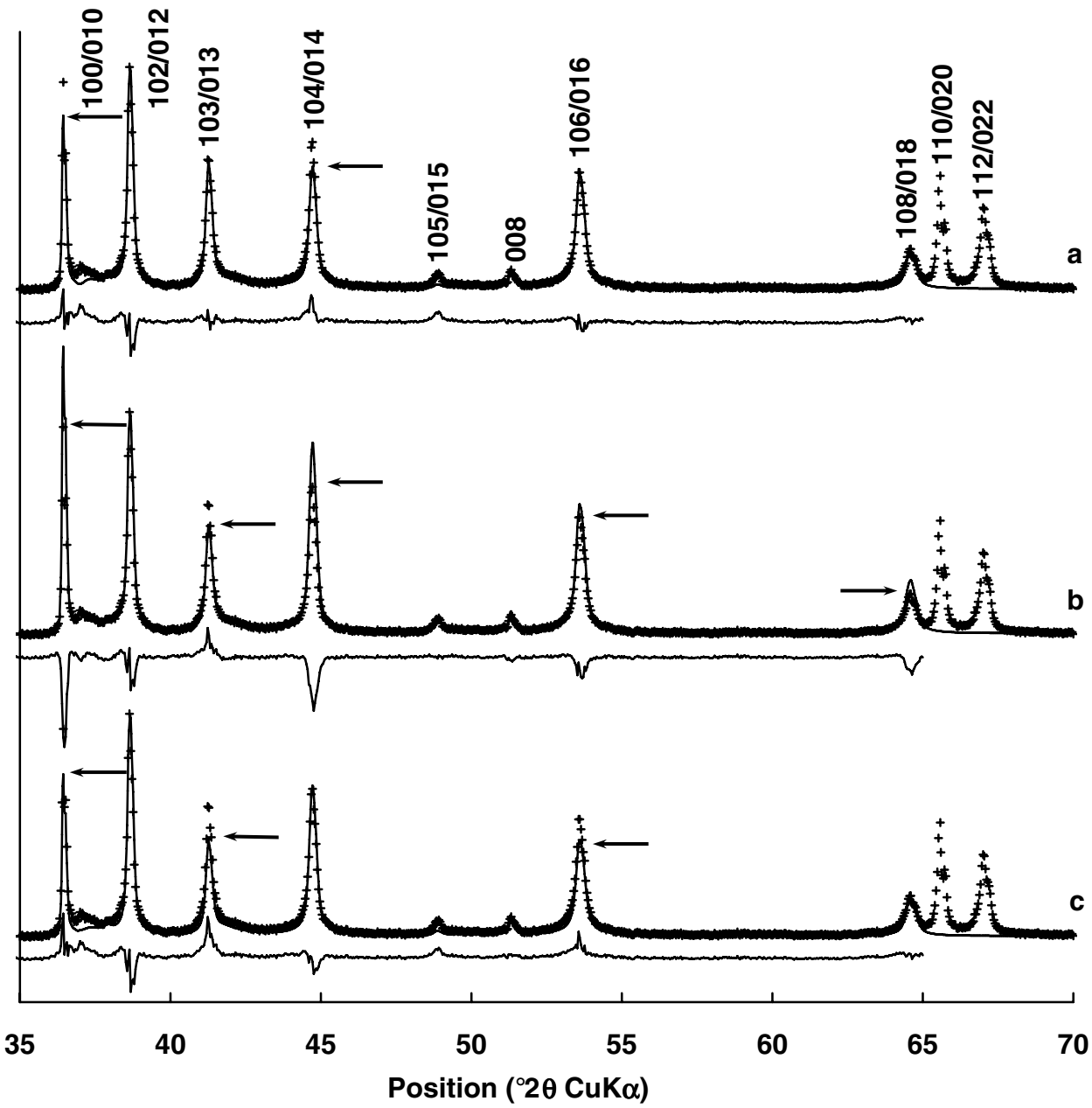

Please print in two column format

Gaillot et al. - Fig. 07

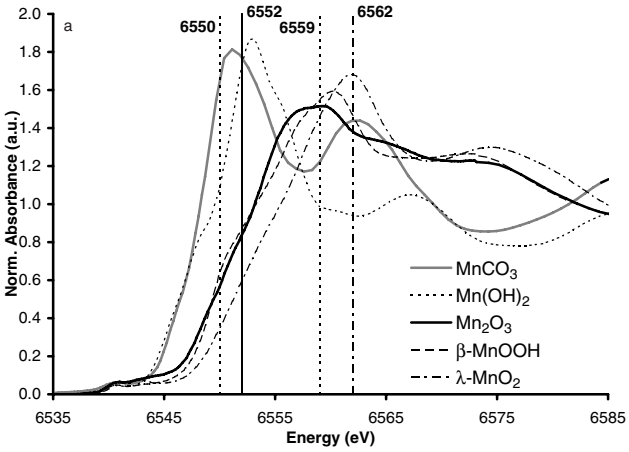

Please print in one column format

Gaillot et al. Fig. 08

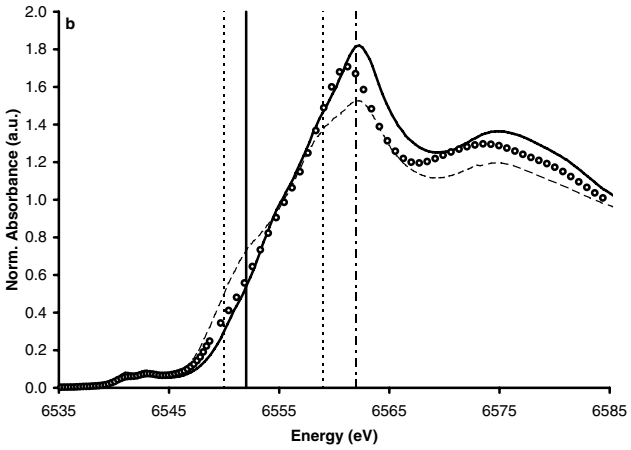

Please print in one column format

Gaillot et al. Fig. 08

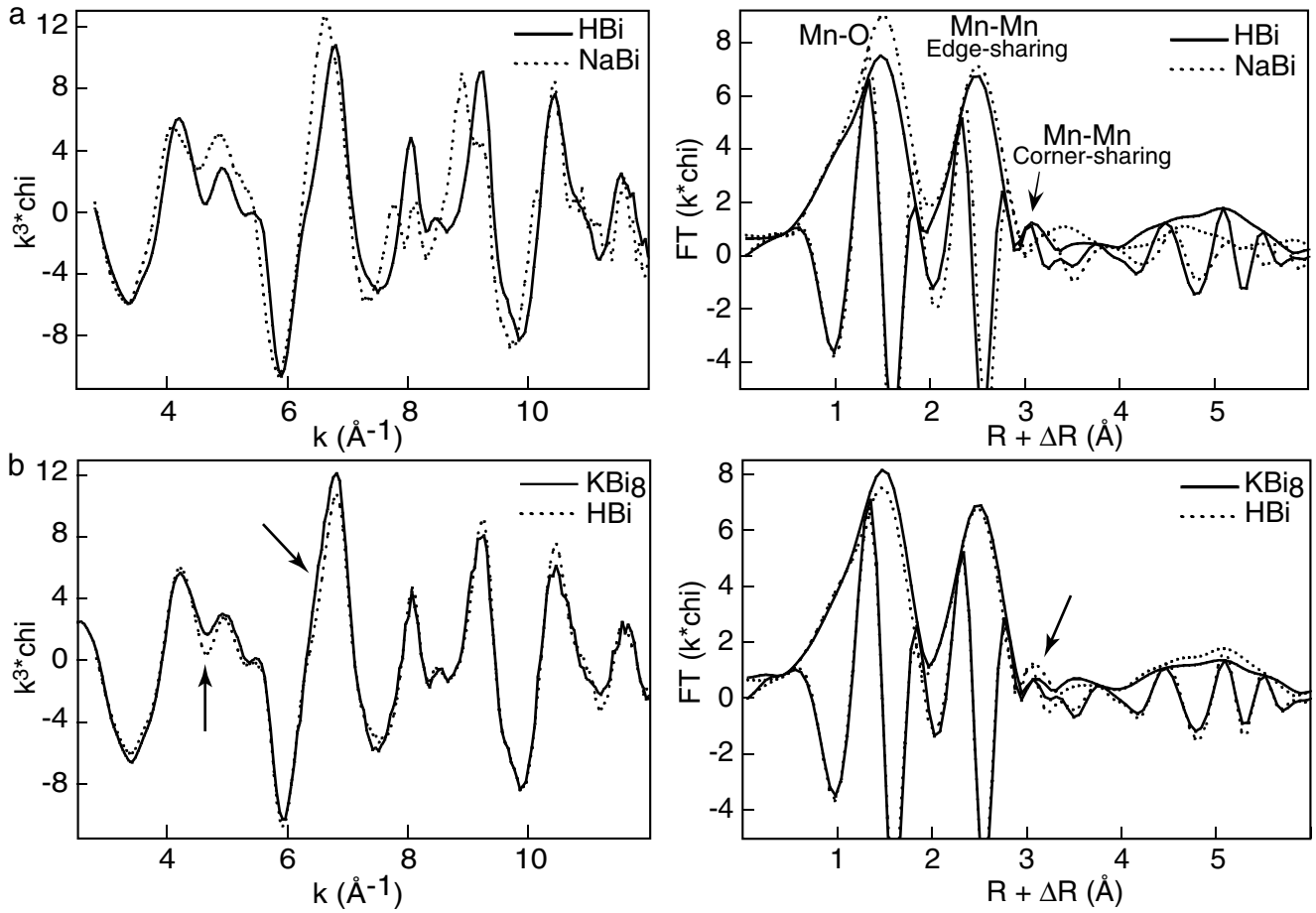

Please print in two column format

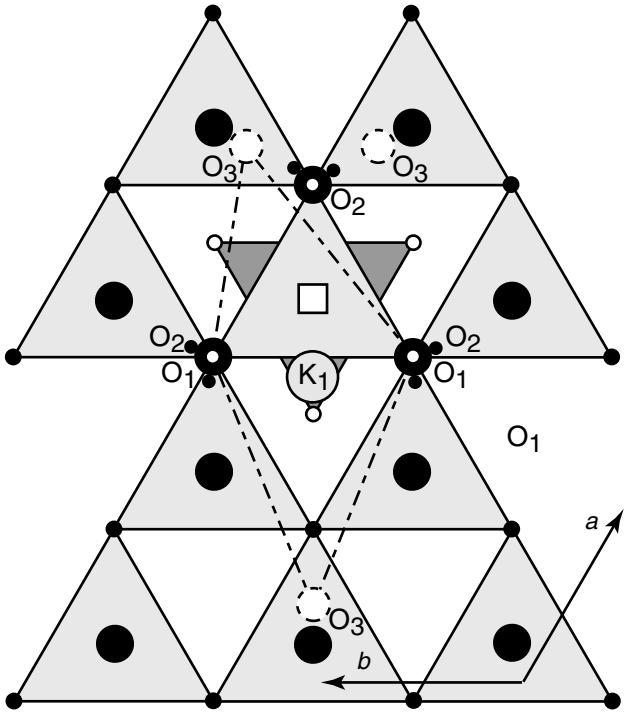

Please print in one column format

Gaillot et al. Fig. 10

For Table of Contents Use Only

Structure of synthetic K-rich birnessite obtained by high-temperature decomposition of $KMnO_4$. Part I. Two-layer polytype from 800°C experiment.

Anne-Claire Gaillot, David Flot, Victor A. Drits, Alain Manceau, Manfred Burghammer, Bruno Lanson

Graphic joined as EPS file

The crystal structure of microcrystalline phyllomanganate birnessite, which was determined from the first time from a single-crystal, consists of edge-sharing $Mn^{4+}O_6$ octahedra building up layers. Vacant layer octahedra are capped on either side by interlayer Mn^{3+} cations (Mn2) having octahedral coordination. Layer charge deficit is compensated for by hydrated (O3) interlayer K^+ cations in prismatic cavities. These cations are shifted from the center of these cavities to provide local charge compensation to O1 atoms.

For table of contents use only

A.-C. Gaillot, D. Flot, V.A. Drits, A. Manceau, M. Burghammer, B. Lanson

Structure of synthetic K-rich birnessite obtained by high-temperature decomposition of KMnO4.

PartI. Two-layer polytype from 800°C experiment.

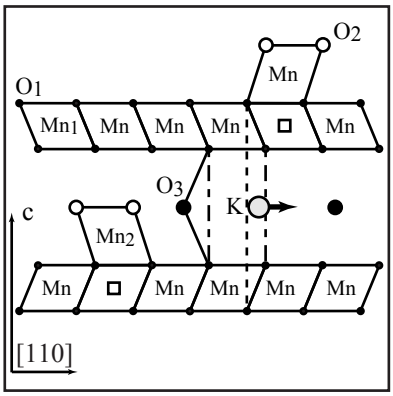

Gaillot et al. Fig. TOC